Spurs in Millimeter-Wave FMCW Radar System-on-Chip

Reza Nikandish, *Senior Member, IEEE*, Alireza Yousefi, *Member, IEEE*, and Elham Mohammadi

***Abstract*— In this article, we present a nonlinear system model to evaluate the impact of circuit nonlinearities on spurs in millimeter-wave frequency-modulated continuous-wave (FMCW) radar system-on-chips. The developed model includes the harmonics of the frequency multiplier, nonlinearity of the power amplifier (PA) and low-noise amplifier (LNA), the switching operation of the receiver (RX) mixer, the limited bandwidth of the PA, LNA, transmitter (TX) and RX antennas, as well as the TX-to-RX leakage. The developed nonlinear model can be used to derive the frequency and amplitude of spurs in the radar IF spectrum. The major insights about the impact of different nonlinearities and their *interactions* are as follows: 1) harmonics of the frequency multiplier appear as spurs in the IF spectrum; 2) PA can be driven in its nonlinear region to mitigate the harmonics generated by the frequency multiplier; 3) bandwidth of the TX and RX systems should be limited to attenuate the undesired harmonics; and 4) interaction between the TX-to-RX leakage signal and the LNA nonlinearity can lead to spurs close to the target echo in the IF spectrum.**

***Index Terms*— Chirp signal, frequency-modulated continuous-wave (FMCW) radar, spurs, millimeter-wave, nonlinearity, self-interference, sensing, system-on-chip (SoC).**

I. Introduction

MILLIMETER-WAVE (mm-wave) high-resolution radars have attracted extensive interests to enhance their performance and leverage their underutilized potentials for a plethora of emerging applications. These radars, extensively explored as automotive sensors, e.g., advanced driver assistance systems (ADAS) and autonomous driving [1], [2], progressively find their way in other applications. These include medical imaging, vital signs monitoring, gesture recognition for human-machine interaction [3], internet of things (IoT) sensors, smart buildings, industrial transport, and robotics.

Recently, extensive developments of mm-wave radar system-on-chip (SoC) have been reported [4], [5], [6], [7], [8], [9], [10], [11], [12], [13], [14], [15], [16], [17], [18], [19], [20], [21], [22], [23]. Continuous-wave radar architectures, especially frequency-modulated continuous-wave (FMCW), are widely used in mm-wave bands. Several designs have been realized using CMOS, silicon-on-insulator (SOI), and silicon-germanium (SiGe) processes, operating at different mm-wave frequencies: 60 GHz, 77 GHz, 76–81 GHz, 140 GHz, and 200–300 GHz [4], [5], [6], [7], [8], [9], [10], [11], [12], [13], [14], [15], [16], [17], [18], [19]. The radar range resolution can be improved by operating at higher mm-wave bands to exploit the available wide bandwidth ($\Delta R \propto 1/B$). A fine range resolution of 54 μm has been achieved using a 250-GHz autodyne FMCW radar implemented in a 55-nm SiGe process [7]. The radar angular resolution can be enhanced using the multi-input multi-output (MIMO) system architecture ($\Delta\Phi \propto 1/N_{\mathrm{TX}}N_{\mathrm{RX}}$) [24], [25]. An angular resolution of 1° has been reported in [15] for a 77/79 GHz phase-modulated continuous-wave (PMCW) radar composed of 12 transmitter (TX) and 8 receiver (RX) channels fabricated using a 28-nm CMOS process. Moreover, 4D gesture sensing has been realized using a 60-GHz FMCW MIMO radar system [4].

Signal generation for high-resolution mm-wave FMCW radars can be quite challenging as a result of stringent requirements on bandwidth, phase noise, jitter, and spurs. The chirp signal can be generated using all-digital or hybrid analog-digital phase-locked loops (PLLs) [31], [32], [33], [34]. Several phase noise and jitter models for the PLL-based FMCW radars have been developed [35], [36], [37], [38]. The chirp nonlinearity effects [28] can be mitigated using digital error correction or calibration techniques. In mm-wave bands, the PLL is usually followed by a frequency multiplier to transform the reference signal to ultimate frequency. The mm-wave frequency multipliers suffer from a low harmonic rejection ratio (HRR) and, as a result, their output harmonics can pass through the radar bandwidth and manifest as spurs in the detected signal spectrum [39].

Furthermore, the nonlinearity of the power amplifier (PA) and low-noise amplifier (LNA) can affect the harmonics level, especially at low supply voltages of nanoscale CMOS processes (e.g., < 1 V). The TX-to-RX leakage signal can drive the RX circuitry (especially the LNA) into gain compression. A comprehensive nonlinear model is, therefore, essential to derive requirements on the circuit components of the FMCW radar for efficient circuit and system designs.

In this article, which is an extension of preliminary results in [40], we present a nonlinear system model for FMCW radars. The model includes several important effects: harmonics of the frequency multiplier, nonlinearity of the PA, LNA, the switching operation of the RX mixer, the limited bandwidth of the TX and RX, the stop-band rejections of the

Manuscript received 11 November 2022; revised 31 January 2023 and 31 March 2023; accepted 4 April 2023. Date of publication 10 April 2023; date of current version 21 April 2023. *(Reza Nikandish and Alireza Yousefi contributed equally to this work.) (Corresponding author: Reza Nikandish.)*

Reza Nikandish is with the School of Electrical and Electronic Engineering, University College Dublin, Dublin, D04 V1W8 Ireland (e-mail: reza.nikandish@ieee.org).

Alireza Yousefi is with Syntiant Corporation, Irvine, CA 92618 USA.

Elham Mohammadi is with Intel Corporation, Hillsboro, OR 97124 USA (e-mail: elham.mohammadi@intel.com).

Digital Object Identifier 10.1109/TRS.2023.3265845

TX, RX, and IF filter, and the TX-to-RX leakage. Moreover, interactions between different nonlinearities are considered in the model. The developed model can be used to estimate the frequency and amplitude of spurs in the radar IF spectrum without the need for time-consuming system and circuit simulations.

The paper is structured as follows. In Section II, the nonlinear model for FMCW radars is presented. The analysis of the radar TX and RX systems is provided in Section III. This is followed by simulations and discussion in Section IV. Finally, the concluding remarks are presented in Section V.

II. Nonlinear System Model of FMCW Radar

A. Principles of FMCW Radar

Architecture of a mm-wave FMCW radar system is shown in Fig. 1. The reference chirp signal is generated at a lower frequency (e.g., 10 GHz) and then is transformed using a frequency multiplier to the ultimate mm-wave band. This approach is useful to achieve lower phase noise in the reference signal. The reference signal can be generated using a chirp PLL, while the frequency multiplier can be realized either as a separate circuit or co-integrated with the PLL as an harmonic extractor. The reference signal has a linear time-dependent frequency which can be described as

$$f_{\text{ref}}(t) = f_0 + St \quad 0 \le t \le T_c, \tag{1}$$

where f_0 is the chirp initial frequency, $S = B/T_c$ is the chirp frequency slope and B is its bandwidth. T_c denotes the chirp repetition period.[1] The instantaneous phase of the chirp signal can be derived as

$$\Phi_{\text{ref}}(t) = 2\pi \int f_{\text{ref}}(t)dt = \Phi_0 + 2\pi f_0 t + \pi S t^2. \tag{2}$$

The multiply-by-N frequency multiplier ideally generate a chirp signal with a frequency of $Nf_{\text{ref}}(t)$. This signal features the bandwidth of NB, the frequency slope of NS, and a repetition period of T_c, the same as the reference signal.

The frequency multiplier output signal is amplified by a PA and is transmitted through the TX antenna. The PA is operated in nonlinear mode to achieve high efficiency, while no nonlinearity constraint is usually imposed on the PA in FMCW radars as it should amplify a constant-envelope signal.

The transmitted signal illuminates the target and reflected back toward the radar receiver. The received signal is related to the transmitted signal as follows:

$$x_{\text{RX}}(t) = G_R x_{\text{TX}}(t - \tau_R), \tag{3}$$

where G_R is the attenuation factor and τ_R denotes the radar signal time-of-flight (ToF). Using the radar range equation, G_R can be derived as

$$G_R = \left(\frac{G_{\text{A,TX}} G_{\text{A,RX}} L_{\text{sys}} \sigma \lambda^2}{(4\pi)^3 R^4}\right)^{\frac{1}{2}}, \tag{4}$$

where $G_{\text{A,TX}}$ and $G_{\text{A,RX}}$ are gain of the TX and RX antennas, L_{sys} is the total system loss, σ is the target radar cross section (RCS), λ is the signal wavelength, and R is the target range [29]. Furthermore, ToF for a static target at the (initial) range R_0 with respect to the radar is given by

$$\tau_{R_0} = \frac{2R_0}{c}. \tag{5}$$

For a moving target, a Doppler frequency shift is also introduced in the received signal, $f_D = 2\ Nf_0 v/c$. This can be modeled by using a time-dependent ToF as follows:

$$\tau_R(t) = \frac{2(R_0 + vt)}{c}, \tag{6}$$

where v is the radial velocity of the target in the direction moving away from the radar.

The received signal is amplified by an LNA and then is mixed by a replica of the frequency multiplier output signal. The mixer output signal, after passing through the IF bandpass filter (BPF), has an instantaneous phase of

$$\Phi_{\text{IF}}(t) = N\Phi_{\text{ref}}(t) - N\Phi_{\text{ref}}(t - \tau_R(t)), \tag{7}$$

which roughly represents a sinusoidal waveform with the frequency of

$$f_{\text{IF}} = (NS)\tau_{R_0} + f_D = \left(\frac{2NS}{c}\right)R_0 + \left(\frac{2Nf_0}{c}\right)v. \tag{8}$$

The target range and velocity can be extracted from the IF spectrum using a two-dimensional Fast Fourier Transform (FFT). The range is detected by applying the FFT to each chirp of the chirp sequence (fast chirp), while the velocity is derived from the FFT of the chirp sequence (slow chirp) as shown in Fig. 1 [25], [26].

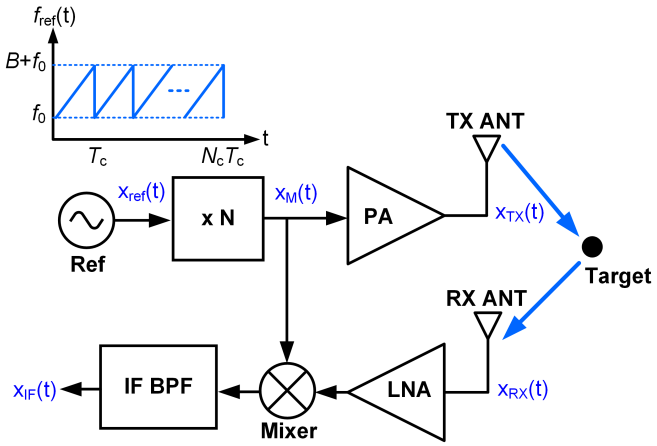

Fig. 1. Architecture of the mm-wave FMCW radar system.

B. FMCW Radar Nonlinear Model

There are several important nonlinear effects in the FMCW radar system which can degrade its performance, e.g., reduced sensitivity, limited dynamic range, and false targets. Some effects are explored in the literature [27], including the chirp nonlinearity [28], jitter [35], phase noise [36], [37], harmonics of the reference signal [39], while some circuit nonlinearities require special attention in emerging integrated radar systems. Therefore, a nonlinear system model which properly captures

[1] It is assumed that the frequency has a sharp return to f_0 at $t = T_c^+$. In practice, the return takes a nonzero time T_r, but usually $T_r \ll T_c$.

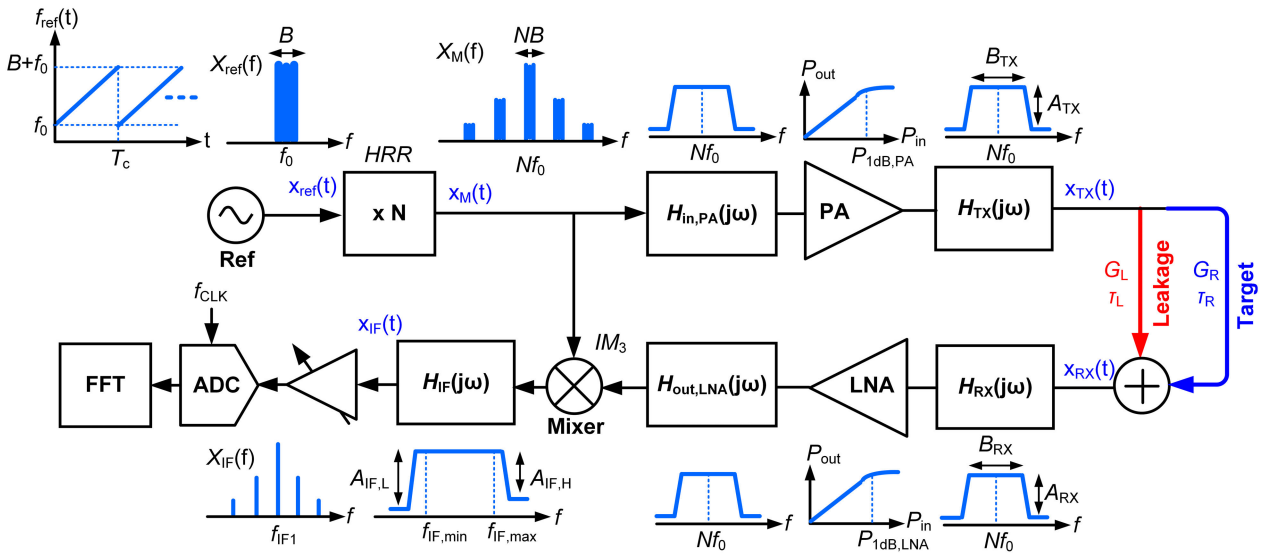

Fig. 2. Proposed nonlinear system model for mm-wave FMCW radar.

the circuit nonlinearities and *interactions of different nonlinear effects with each other* can be very valuable for efficient design of a mm-wave FMCW radar SoC.

We propose a nonlinear system model for mm-wave FMCW radars as shown in Fig. 2. The main effects included in this model are as follows.

1) *Output Harmonics of the Frequency Multiplier*: The frequency multiplier generates harmonics other than the desired N-th harmonic of the reference signal. We neglect spurs generated by the reference circuits, e.g., fractional-N PLL, direct digital synthesizer (DDS). Spurs estimation and mitigation methods for different types of frequency synthesizers are extensively investigated in the literature [41], [42], [43], [44]. In this paper we focus on spurs generated by the radar blocks. Therefore, the level of harmonics depends on the multiplier circuit structure, frequency band, the chirp bandwidth, quality factor of passive components, and features of the integrated circuit process. HRR levels in the order of $\sim$30–50 dBc are reported in mm-wave bands using different circuit structures, e.g., harmonic tuning, harmonic mixing, push-push, and injection locking [47], [48], [49], [50], [51]. In practical mm-wave FMCW radars however it is difficult to achieve a high HRR, typically >20 dBc, across a wide modulation bandwidth, particularly if the frequency multiplication factor is large and more harmonics should be suppressed. The output signal of the frequency multiplier can be considered as

$$x_{\text{out,MUL}}(t) = \sum_{k=1}^{\infty} a_k \cos[k\Phi_{\text{ref}}(t)]. \tag{9}$$

It is assumed that the harmonics are in phase to simplify the analysis.[2] In practice, only a few harmonics close to the desired harmonic N needs to be considered. This depends on bandwidth of the multiplier and subsequent TX circuits (i.e., PA and TX antenna) and the frequency difference of the harmonics. Furthermore, it is assumed that HRR of the frequency multiplier remains constant across the bandwidth.

2) *Nonlinearity of the PA*: In FMCW radars, the PA nonlinearity is usually overlooked as its input signal has a constant amplitude. However, the PA nonlinearity can be important when we consider the harmonics of the reference signal. The PA nonlinearity results in *spectral regrowth* which spreads the harmonics in a wide bandwidth and can alter their relative amplitude with respect to the fundamental signal [30]. As a result, HRR in output of the PA can be different with HRR in output of the frequency multiplier. We consider the third-order polynomial output-input characteristic for the PA as follows

$$x_{\text{out,PA}}(t) = \alpha_{1,\text{PA}} x_{\text{in,PA}}(t) + \alpha_{3,\text{PA}} x^3_{\text{in,PA}}(t). \tag{10}$$

It is assumed that the PA is realized as a differential circuit and even-order harmonics of its output signal are negligible. For a typical compressive output-input characteristic, $\alpha_{1,\text{PA}}$ and $\alpha_{3,\text{PA}}$ have opposite signs. Furthermore, the input-referred 1-dB compression point of the PA can be related to the polynomial coefficients as [30]

$$P_{1\text{dB,PA}} = \frac{4}{3}\beta \left|\frac{\alpha_{1,\text{PA}}}{\alpha_{3,\text{PA}}}\right|, \tag{11}$$

$$\beta = 1 - 10^{-\frac{1}{20}} \approx 0.11. \tag{12}$$

A constant $P_{1\text{dB,PA}}$ is assumed across the bandwidth to simplify the analysis.

3) *Bandwidth of the PA and TX Antenna*: Bandwidth of the PA determines how output harmonics of the frequency multiplier reach to the TX antenna and are transmitted to the target.[3] We use two transfer functions $H_{\text{in,PA}}(j\omega)$ and $H_{\text{out,PA}}(j\omega)$ to model the frequency response of the PA input and output matching networks, as shown in Fig. 2. The two

[2]The phase difference between the harmonics can be controlled through circuit design techniques to mitigate undesired harmonics and improve the HRR of the frequency multiplier.

[3]Spectrum of chirp signal is dependent on its time-bandwidth product $T_c B$. For large values, e.g., $T_c B > 100$, it approaches a rectangular shape with bandwidth of B [52].

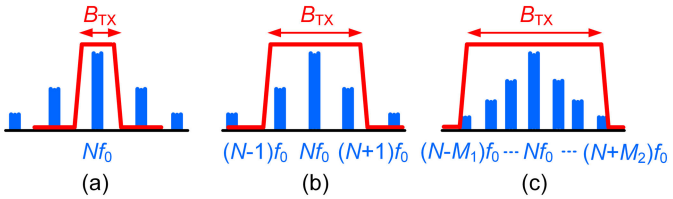

Fig. 3. Three scenarios for the number of harmonics which can pass through the transmitter bandwidth.

transfer functions are necessary to properly model the spectral components which can enter the PA nonlinear core and the spurs present at the PA output signal. The PA bandwidth is practically limited by its output matching network which provides the optimal load resistance to the transistors to achieve the maximum output power or efficiency. The PA output and TX antenna frequency-domain transfer functions can therefore be merged and modeled as the TX frequency response

$$H_{\mathrm{TX}}(j\omega) = H_{\mathrm{out,PA}}(j\omega)H_{\mathrm{ANT,TX}}(j\omega). \tag{13}$$

The TX output signal $x_{\mathrm{TX}}(t)$ is achieved after applying $H_{\mathrm{TX}}(j\omega)$ on the fundamental and harmonic components of the PA output signal $x_{\mathrm{out,PA}}(t)$. Three possible scenarios are shown in Fig. 3.[4] Fig. 3(a) shows the case that the TX has a narrow bandwidth (B_{TX}) or spacing between harmonics is too wide, i.e., $B_{\mathrm{TX}} < 2f_0$. In this condition, only the desired harmonic N should be considered as the other harmonics are substantially suppressed. In Fig. 3(b), the TX bandwidth allows transmission of the harmonic N and two adjacent harmonics $N \pm 1$ (i.e., $2f_0 < B_{\mathrm{TX}} < 4f_0$). Finally, as shown in Fig. 3(c), when the TX has a wide bandwidth or harmonic spacing is narrow, i.e., $B_{\mathrm{TX}} > 4f_0$, several harmonics fall within the TX bandwidth. In this paper, we consider the case where only adjacent harmonics are located in the TX bandwidth [Fig. 3(b)] to simplify the derivations. It is also assumed that in practical conditions $H_{\mathrm{in,PA}}$ has a bandwidth close to that of $H_{\mathrm{out,PA}}$ and variations in the amplitude response of the PA and TX antenna are ignored. In practice, usually the harmonics close to the main output harmonic have the largest relative magnitude and cannot be directly filtered. The insights that will be provided can be extended to the general case of multiple harmonics located in the TX bandwidth. The relative attenuation of the harmonic k can be derived as

$$A_{\mathrm{TX,k}} = \frac{|H_{\mathrm{TX}}(jk\omega_0)|}{|H_{\mathrm{TX}}(jN\omega_0)|}, \tag{14}$$

which is dependent on the frequency difference between the signal components, the quality factor of on-chip passive elements used in the PA circuit, and the TX antenna bandwidth. In the condition that the harmonics $N \pm 1$ are too close to the harmonic N, $A_{\mathrm{TX}} \approx 1$.

4) *TX-to-RX Leakage Signal*: The leakage signal from the TX to RX, arising from coupling between their antennas or coupling through the chip substrate, can have a power much higher than the received signal power which desensitizes the RX circuits (especially the LNA) and masks the target. Therefore, the leakage cancellation is an important challenge in FMCW radar SoC. The leakage cancellation in the order of ∼30–50 dB has been achieved using different approaches developed for integrated radar systems [5], [6], [18], [19], [20], [21], [22]. The imperfect leakage cancellation can limit performance of the radar system. We use the following model to describe the received signal:

$$x_{\mathrm{RX}}(t) = G_R x_{\mathrm{TX}}(t - \tau_R) + G_L x_{\mathrm{TX}}(t - \tau_L), \tag{15}$$

where G_L is a factor indicating strength of the leakage signal and τ_L is its delay relative to the TX signal. The parameters G_L and τ_L are independent of the target range, while G_R and τ_R are range-dependent. As a result, the significance of the leakage can be different for short and long target ranges. Moreover, it is assumed that the leakage signal power remain constant across the bandwidth of interest.

5) *Nonlinearity of the LNA*: The LNA nonlinearity can become important for close targets with strong reflected signal or when there is a large leakage signal. In these conditions, the LNA can experience severe gain compression or even saturation. Furthermore, the LNA nonlinearity can change the relative amplitudes of the harmonics in the TX signal. We use a third-order polynomial, similar to the PA, to describe the LNA nonlinearity:

$$x_{\mathrm{out,LNA}}(t) = \alpha_{1,\mathrm{LNA}} x_{\mathrm{in,LNA}}(t) + \alpha_{3,\mathrm{LNA}} x^3_{\mathrm{in,LNA}}(t). \tag{16}$$

This can be used to derive a limit on the minimum target range (i.e., maximum G_R), the maximum tolerable leakage signal, and the required input-referred 1-dB compression point of the LNA, $P_{\mathrm{1dB,LNA}}$. We assume a constant $P_{\mathrm{1dB,LNA}}$ over the bandwidth to simplify the derivations, while in a realistic implementation it can change with frequency.

6) *Bandwidth of the LNA and RX Antenna*: Bandwidth of the LNA and RX antenna determines the received signal harmonics which can reach to the mixer. The LNA is modeled by two transfer functions $H_{\mathrm{in,LNA}}(j\omega)$ and $H_{\mathrm{out,LNA}}(j\omega)$ which respectively model the frequency responses of the input and output matching network (Fig. 2). The LNA bandwidth is mainly limited by its input matching network which is responsible for providing the optimum noise matching to the transistor. The RX antenna and the LNA input transfer functions can therefore be effectively modeled by an RX transfer function

$$H_{\mathrm{RX}}(j\omega) = H_{\mathrm{in,LNA}}(j\omega)H_{\mathrm{ANT,RX}}(j\omega). \tag{17}$$

We use the model shown in Fig. 3(b) for the RX frequency response (the same as for the TX). It is assumed that bandwidth of $H_{\mathrm{out,LNA}}$ is close to that of $H_{\mathrm{in,LNA}}$. Moreover, variations in the LNA and RX antenna amplitude across the bandwidth are neglected.

The harmonic components can be present in both of the received and leakage signals. We consider the fundamental component N and its adjacent harmonics $N \pm 1$. The relative attenuation of the harmonic k is given by

$$A_{\mathrm{RX,k}} = \frac{|H_{\mathrm{RX}}(jk\omega_0)|}{|H_{\mathrm{RX}}(jN\omega_0)|}. \tag{18}$$

[4]The practical condition $B \ll f_0$ is applied.

7) *Switching Operation of the Mixer*: The mixer mainly downconverts the LNA output signal by mixing it with a replica of the multiplier output signal. The IF BPF passes the frequency band $f_{\mathrm{IF,min}} \leq f \leq f_{\mathrm{IF,max}}$, where $f_{\mathrm{IF,min}}$ and $f_{\mathrm{IF,max}}$ respectively correspond to the minimum and maximum target range. The mixer switching operation leads to intermodulation distortion (IMD) components, which can mix different harmonics present in the reference signal and the LNA output signal to produce some spectral components in the IF band.

8) *Bandwidth and Attenuation of the IF Filter*: The IF filter is modeled as an BPF in Fig. 2, while it is practically realized as a leakage cancellation high-pass filter (HPF) followed by an anti-aliasing low-pass filter (LPF) [8], [9]. These two filters can have different circuit implementations. The IF BPF has a bandwidth which covers the IF frequencies corresponding to the minimum to maximum target ranges, i.e., $f_{\mathrm{IF,min}} \leq f \leq f_{\mathrm{IF,max}}$, while its lower cut-off frequency can be much lower than $f_{\mathrm{IF,min}}$ to meet the leakage cancellation requirements. It is assumed that the IF BPF provides an attenuation of $A_{\mathrm{IF,L}}$ in its lower stop band and $A_{\mathrm{IF,H}}$ in the upper stop band.

The IF filter, as well as the TX and RX equivalent filters, can exhibit amplitude variations in their pass band. In the condition that the chirp signal bandwidth is much narrower than the filter bandwidth, e.g., $NB \ll B_{\mathrm{TX}}$ in Fig. 3(b), such variations can be neglected. However, if bandwidth of the chirp signal is comparable with the filter bandwidth, e.g., $NB \sim B_{\mathrm{TX}}$ in Fig. 3(a), these variations can distort the chirp signal and lead to undesired amplitude and phase modulations.

C. Model Limitations

The proposed model for mm-wave FMCW radars inevitably has some limitations arising from higher order imperfections which are excluded for the sake of clarity but can have some implications under certain practical conditions. We briefly discuss the most important effects which should be taken into account for an accurate evaluation of the radar performance.

1) A broadband frequency multiplier can exhibit large variations in the amplitude of the fundamental and harmonics across the bandwidth [48], [49]. This behavior cannot be described by a constant HRR across the bandwidth. In this case, an average or worst-case HRR can be used in the developed radar model.
2) The largest harmonics of the frequency multiplier can be other than the adjacent harmonics $N \pm 1$. These harmonics usually are located far from the center frequency of the circuits and are attenuated by the PA, LNA, and TX/RX antennas. Nevertheless, a slightly revised analysis can be applied in this case.
3) The nonlinear properties of the PA and LNA can significantly change across the radar bandwidth. Using a frequency-dependent P_{1dB} however will make the system analysis intractable. It is possible to use an average P_{1dB} across the bandwidth to achieve more accurate results. In the forthcoming analysis, it is assumed that the leakage signal power is not such high that saturates the LNA circuit. This permits the LNA nonlinearity to be modeled by a third-order polynomial to simplify the derivations and obtain intuitive results.
4) Spurs in the reference signal are neglected in the analysis to focus on the spurs generated by the radar. In a radar SoC with integrated chirp synthesizer, e.g., a fractional-N PLL, the spurs can be produced through different mechanisms including the quantization noise and its downconversion by the nonlinear phase detector [41], self modulation and quantization noise folding [42]. A more complete radar model should also include impacts of the incoming spurs.

III. Analysis of FMCW Radar System

We use the nonlinear system model for FMCW radar to investigate spectral contents of signals at the output of the TX, the input of the RX, and the IF.

A. Analysis of Transmitter

The frequency multiplier output signal is generally given by (9). We consider the desired harmonic N and two adjacent harmonics $N \pm 1$. Furthermore, it is assumed that the two harmonics have the same amplitude to simplify the derivations (in the worst-case condition, this amplitude can be considered as the largest amplitude of two harmonics). Therefore, the multiplier output signal can be written as[5]

$$x_{\mathrm{out,MUL}}(t) = a_{\mathrm{N}}[\cos(N\Phi) + k_{\mathrm{ref}}\cos[(N \pm 1)\Phi]], \qquad (19)$$

where a_{N} is amplitude of the desired harmonic N, k_{ref} is relative amplitude of the harmonics $N \pm 1$ with respect to the harmonic N, and $\Phi = \Phi_{\mathrm{ref}}(t)$ is the instantaneous phase of the reference signal. The notation $\cos[(N \pm 1)\Phi] = \cos[(N + 1)\Phi] + \cos[(N - 1)\Phi]$ is used to simplify mathematical derivations. The parameter k_{ref} is related to HRR of the frequency multiplier as $HRR = -20\log_{10}(k_{\mathrm{ref}})$. This signal appears as the input signal of the PA, with a scaled amplitude A_{in} due to power division between the PA and mixer. Using the PA nonlinear characteristic (10) with the frequency multiplier output given by (19) as its input signal, it can be shown that the PA output signal $x_{\mathrm{out,PA}}(t)$ has spectral components at $N\Phi$, $3N\Phi$, $(N \pm 1)\Phi$, $(N \pm 2)\Phi$, $(N \pm 3)\Phi$, $(3N \pm 1)\Phi$, $(3N \pm 2)\Phi$, and $(3N \pm 3)\Phi$. This indicates that the PA output spectrum which includes the main component spans from $(N - 3)\Phi$ to $(N + 3)\Phi$, which is three times wider than the input spectrum span (*spectral regrowth*).

We assume that the TX bandwidth allows transmission of the desired harmonic N and its two adjacent harmonics $N \pm 1$ with the same relative attenuation of $A_{\mathrm{TX,N\pm1}} = A_{\mathrm{TX}}$. The TX system, in the strict sense, is a dynamic nonlinear system which its rigorous analysis requires the use of nonlinear approaches, e.g., the Wiener series [53]. These methods however will result in complicated derivations [30, Ch. 2]. Instead, we use a simplified approach where the TX system is decomposed into a frequency-independent nonlinear model followed by a linear band-limited frequency response (see Fig. 2).

[5]It is assumed that there is no phase offset between the three harmonics to simplify theoretical derivations.

Therefore, using (10), (19), and applying the discussed transmitter's bandwidth limitations, the transmitted signal can be derived as[6]

$$x_{\mathrm{TX}}(t) = a_{\mathrm{TX}}[\cos(N\Phi) + k_{\mathrm{TX}}\cos[(N\pm 1)\Phi]], \tag{20}$$

where a_{TX} and k_{TX} are given by

$$a_{\mathrm{TX}} = \alpha_{1,\mathrm{PA}}A_{\mathrm{in}} + \frac{3}{4}(1+6k_{\mathrm{ref}}^2)\alpha_{3,\mathrm{PA}}A_{\mathrm{in}}^3, \tag{21}$$

$$k_{\mathrm{TX}} = \left(\frac{\alpha_{1,\mathrm{PA}}A_{\mathrm{in}} + \frac{9}{4}(1+k_{\mathrm{ref}}^2)\alpha_{3,\mathrm{PA}}A_{\mathrm{in}}^3}{\alpha_{1,\mathrm{PA}}A_{\mathrm{in}} + \frac{3}{4}(1+6k_{\mathrm{ref}}^2)\alpha_{3,\mathrm{PA}}A_{\mathrm{in}}^3}\right)A_{\mathrm{TX}}k_{\mathrm{ref}}. \tag{22}$$

The PA usually has a compressive nonlinear gain behavior which requires $\alpha_{1,\mathrm{PA}}$ and $\alpha_{3,\mathrm{PA}}$ to have opposite signs. Therefore, using (11), $\alpha_{3,\mathrm{PA}}$ can be expressed as $\alpha_{3,\mathrm{PA}} = -(4/3)\beta\alpha_{1,\mathrm{PA}}/P_{1\mathrm{dB,PA}}$. The input power of the PA can be related to its input signal amplitude as $P_{\mathrm{in,PA}} = A_{\mathrm{in}}^2$. Using these relations and applying the practical condition $k_{\mathrm{ref}}^2 \ll 1$, (21) and (22) can be simplified to

$$a_{\mathrm{TX}} \approx \alpha_{1,\mathrm{PA}}A_{\mathrm{in}}\left(1-\beta\frac{P_{\mathrm{in,PA}}}{P_{1\mathrm{dB,PA}}}\right), \tag{23}$$

$$k_{\mathrm{TX}} \approx \left(\frac{1-3\beta\frac{P_{\mathrm{in,PA}}}{P_{1\mathrm{dB,PA}}}}{1-\beta\frac{P_{\mathrm{in,PA}}}{P_{1\mathrm{dB,PA}}}}\right)A_{\mathrm{TX}}k_{\mathrm{ref}}. \tag{24}$$

It is noted that the harmonics level at the output of the PA is also dependent on gain compression[7] and frequency response. This indicates that in certain conditions, dependent on the quality factor of on-chip passive elements and the operating frequency, a filter can be embedded in the PA circuit [45] or in the antenna radiating structure [46] to further suppress the undesired harmonics.

It is noted that always $k_{\mathrm{TX}} < k_{\mathrm{ref}}$, indicating that the harmonics level is decreased at output of the TX. For $P_{\mathrm{in,PA}} = P_{1\mathrm{dB,PA}}$, $k_{\mathrm{TX}} \approx 0.75A_{\mathrm{TX}}k_{\mathrm{ref}}$, leading to $\sim$2.5 dB lower harmonics. *This insight indicates that it is beneficial to drive the PA in nonlinear region to mitigate harmonics generated by the frequency multiplier and to improve the PA efficiency.*

B. Analysis of Receiver

The received signal is composed of the target echo signal and the TX-to-RX leakage signal as indicated by (15). If we consider the frequency multiplier signal as (19), the three harmonics N and $N\pm 1$ will be present in $x_{\mathrm{TX}}(t)$ and, as a result, in both the echo and leakage signals. We consider two cases to provide useful insights.

1) No Leakage Signal: In the condition that the leakage signal is negligible, $G_L \ll G_R$, and assuming that the RX bandwidth only allows the harmonics N and $N\pm 1$ to pass, while the harmonics $N\pm 1$ are attenuated by the factor of A_{RX}, the LNA output signal can be derived as

$$x_{\mathrm{out,LNA}}(t) = a_{\mathrm{out,LNA}}[\cos[N\Phi(t-\tau_R)] + k_{\mathrm{RX}}\cos[(N\pm 1)\Phi(t-\tau_R)]], \tag{25}$$

where $a_{\mathrm{out,LNA}}$ and k_{RX} are given by

$$a_{\mathrm{out,LNA}} \approx \alpha_{1,\mathrm{LNA}}G_R a_{\mathrm{TX}}\left(1-\beta\frac{P_{\mathrm{in,LNA}}}{P_{1\mathrm{dB,LNA}}}\right), \tag{26}$$

$$k_{\mathrm{RX}} \approx \left(\frac{1-3\beta\frac{P_{\mathrm{in,LNA}}}{P_{1\mathrm{dB,LNA}}}}{1-\beta\frac{P_{\mathrm{in,LNA}}}{P_{1\mathrm{dB,LNA}}}}\right)A_{\mathrm{RX}}k_{\mathrm{TX}}. \tag{27}$$

It is noted that the harmonics level is scaled based on (24) and (27) as the reference signal experiences nonlinearity of the PA and LNA.

This signal is mixed with the frequency multiplier output signal. The mixer generates the second-order nonlinear components at $N[\Phi(t)\pm\Phi(t-\tau_R)]$, $(N-1)[\Phi(t)\pm\Phi(t-\tau_R)]$, and $(N+1)[\Phi(t)\pm\Phi(t-\tau_R)]$. Generally, the mixer switching operation leads to spurs with an instantaneous phase which is a linear superposition of two terms from the set $N\Phi(t)$, $N\Phi(t-\tau_R)$, $(N\pm 1)\Phi(t)$, $(N\pm 1)\Phi(t-\tau_R)$. From these components, only $mN[\Phi(t)-\Phi(t-\tau_R)]$, $m(N-1)[\Phi(t)-\Phi(t-\tau_R)]$, and $m(N+1)[\Phi(t)-\Phi(t-\tau_R)]$ (where $m\in\mathbb{Z}$) can pass through the IF BPF, while other components with a spectrum at higher frequencies are suppressed. For $m=1$, these components are amplified by the mixer conversion gain, while for $m\geq 2$ they are attenuated. Therefore, the IF signal can be derived as

$$x_{\mathrm{IF}}(t) = a_{\mathrm{IF}}[\cos[N\Psi_1(t)] + k_{\mathrm{ref}}k_{\mathrm{RX}}\cos[(N\pm 1)\Psi_1(t)]], \tag{28}$$

where $a_{\mathrm{IF}} = G_{\mathrm{c,mix}}a_{\mathrm{out,LNA}}$ is amplitude of the main IF component, $G_{\mathrm{c,mix}}$ is the mixer conversion gain, and $\Psi_1(t)$ is defined as

$$\Psi_1(t) = \Phi(t) - \Phi(t-\tau_R). \tag{29}$$

This reveals two important results. First, *the spurs level at the IF is lower than the original harmonics level of the reference signal.* Using (24) and (27), $k_{\mathrm{IF}} = k_{\mathrm{ref}}k_{\mathrm{RX}}$ can be derived as

$$k_{\mathrm{IF}} \approx \left(\frac{1-3\beta\frac{P_{\mathrm{in,LNA}}}{P_{1\mathrm{dB,LNA}}}}{1-\beta\frac{P_{\mathrm{in,LNA}}}{P_{1\mathrm{dB,LNA}}}}\right)\left(\frac{1-3\beta\frac{P_{\mathrm{in,PA}}}{P_{1\mathrm{dB,PA}}}}{1-\beta\frac{P_{\mathrm{in,PA}}}{P_{1\mathrm{dB,PA}}}}\right)A_{\mathrm{RX}}A_{\mathrm{TX}}k_{\mathrm{ref}}^2. \tag{30}$$

The second result is that *the IF spectrum includes a spectral component at $NS\tau_R$ and two extra components at $(N\pm 1)S\tau_R$*, as shown in Fig. 4(a), where

$$f_{\mathrm{IF1}} = NS\tau_R, \tag{31}$$

$$f_{\mathrm{IF2}} = (N+1)S\tau_R, \tag{32}$$

$$f_{\mathrm{IF3}} = (N-1)S\tau_R. \tag{33}$$

These extra components can lead to overlap between the IF spectra of the echo signals for two close targets and degrade the range resolution of the radar.

[6]If we consider a second-order nonlinearity term in the PA characteristic, $\alpha_{2,\mathrm{PA}}x_{\mathrm{in,PA}}^2(t)$, it can be shown that it will generate spectral components at DC, $2N\Phi$, $(2N\pm 1)\Phi$, and $(2N\pm 2)\Phi$. Fortunately, these components fall outside of the PA bandwidth.

[7]In general, the input power can be normalized to the n-dB compression point of the PA by redefining β as $\beta = 1-10^{-\frac{n}{20}}$.

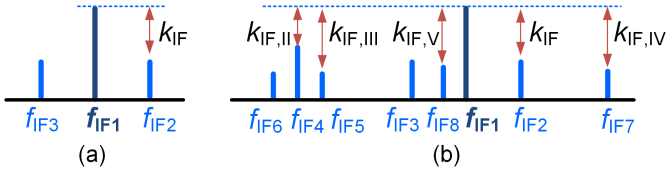

Fig. 4. A typical IF spectrum for single target corresponding to f_{IF1}: (a) with the reference signal harmonics, (b) with the reference signal harmonics and the TX-to-RX leakage.

2) With Leakage Signal: In the presence of leakage signal, the RX system can be considered as a dual-input nonlinear system [54]. The nonlinear interactions between the two input signals can lead to the generation of extra spur components. The LNA input signal is composed of the echo and leakage signals

$$x_{\text{in,LNA}}(t) = x_{\text{echo}}(t) + x_{\text{leak}}(t), \tag{34}$$

where the echo and leakage signals are respectively given by

$$\begin{aligned} &x_{\text{echo}}(t) \\ &= G_R a_{\text{TX}}[\cos[N\Phi(t-\tau_R)] + k_{\text{TX}}\cos[(N\pm 1)\Phi(t-\tau_R)]], \end{aligned} \tag{35}$$

$$\begin{aligned} &x_{\text{leak}}(t) \\ &= G_L a_{\text{TX}}[\cos[N\Phi(t-\tau_L)] + k_{\text{TX}}\cos[(N\pm 1)\Phi(t-\tau_L)]]. \end{aligned} \tag{36}$$

The RX system can be modeled as shown in Fig. 5, where the LNA nonlinearity is considered as two paralleled sub-blocks with characteristics of $y = \alpha_1 x$ and $y = \alpha_3 x^3$. The LNA frequency response which was modeled by the linear transfer function $H_{\text{RX}}(j\omega)$ can be placed in two paralleled paths. We are interested in the components that can pass through the LNA bandwidth and after mixing with one of the terms in the frequency multiplier signal (9), i.e., $N\Phi(t)$ or $(N \pm 1)\Phi(t)$, can pass the IF BPF to appear in the IF spectrum. The linear sub-block generates two signals $\alpha_{1,\text{LNA}} x_{\text{echo}}(t)$ and $\alpha_{1,\text{LNA}} x_{\text{leak}}(t)$ which have the same spectral components as in (35) and (36). The nonlinear sub-block, however, produces four signals $\alpha_{3,\text{LNA}} x^3_{\text{echo}}(t)$, $\alpha_{3,\text{LNA}} x^3_{\text{leak}}(t)$, $3\alpha_{3,\text{LNA}} x^2_{\text{echo}}(t) x_{\text{leak}}(t)$, and $3\alpha_{3,\text{LNA}} x_{\text{echo}}(t) x^2_{\text{leak}}(t)$.

Using the practical approximation $k^2_{\text{TX}} \ll 1$, it can be shown that the nonlinear term $\alpha_{3,\text{LNA}} x^3_{\text{echo}}(t)$ includes the spectral components of $N\Phi(t-\tau_R)$, $(N\pm 1)\Phi(t-\tau_R)$, $3N\Phi(t-\tau_R)$, and $(3N\pm 1)\Phi(t-\tau_R)$.[8] Similarly, the nonlinear term $\alpha_{3,\text{LNA}} x^3_{\text{leak}}(t)$ includes the spectral components of $N\Phi(t-\tau_L)$, $(N\pm 1)\Phi(t-\tau_L)$, $3N\Phi(t-\tau_L)$, and $(3N\pm 1)\Phi(t-\tau_L)$. As we have assumed that the RX frequency response allows only the spectral components Nf_0 and $(N\pm 1)f_0$ to pass [see Fig. 3(b)], these two nonlinear terms only generate the spectral components $N\Phi(t-\tau_R)$, $(N\pm 1)\Phi(t-\tau_R)$, $N\Phi(t-\tau_L)$, and $(N\pm 1)\Phi(t-\tau_L)$, with modified amplitudes.

The other nonlinear terms $3\alpha_{3,\text{LNA}} x^2_{\text{echo}}(t) x_{\text{leak}}(t)$ and $3\alpha_{3,\text{LNA}} x_{\text{echo}}(t) x^2_{\text{leak}}(t)$ can produce new spectral components at linear suppositions of $\Phi(t-\tau_R)$ and $\Phi(t-\tau_L)$. Specifically, it can be shown that the spectral components generated by $x^2_{\text{echo}}(t) x_{\text{leak}}(t)$ which can pass through the RX band are located at $N\Phi(t-\tau_L)$, $(N\pm 1)\Phi(t-\tau_L)$, and $2N\Phi(t-\tau_R) - N\Phi(t-\tau_L)$.[9] Similarly, $x_{\text{echo}}(t) x^2_{\text{leak}}(t)$ leads to the spectral components at $N\Phi(t-\tau_R)$, $(N\pm 1)\Phi(t-\tau_R)$, and $N\Phi(t-\tau_R) - 2N\Phi(t-\tau_L)$.

It can be shown that the LNA output signal can be approximately derived as[10]

$$\begin{aligned} &x_{\text{out,LNA}}(t) \\ &\approx G_R a_{\text{TX}}[C_1\cos[N\Phi(t-\tau_R)] \\ &\quad + C_2\cos[(N\pm 1)\Phi(t-\tau_R)] \\ &\quad + C_3\cos[N\Phi(t-\tau_L)] + C_4\cos[(N\pm 1)\Phi(t-\tau_L)] \\ &\quad + C_5\cos[2N\Phi(t-\tau_R) - N\Phi(t-\tau_L)] \\ &\quad + C_6\cos[N\Phi(t-\tau_R) - 2N\Phi(t-\tau_L)]], \end{aligned} \tag{37}$$

where the coefficients C_1–C_6 are given by

$$C_1 = \alpha_{1,\text{LNA}} A_{\text{in}} + \frac{3}{4}(1+2r^2)\alpha_{3,\text{LNA}} A^3_{\text{in}}, \tag{38}$$

$$C_2 = \alpha_{1,\text{LNA}} A_{\text{in}} k_{\text{TX}} + \frac{3}{4}(3+2r^2)\alpha_{3,\text{LNA}} A^3_{\text{in}} k_{\text{TX}}, \tag{39}$$

$$C_3 = r\alpha_{1,\text{LNA}} A_{\text{in}} + \frac{3}{4}(2r+r^3)\alpha_{3,\text{LNA}} A^3_{\text{in}}, \tag{40}$$

$$C_4 = r\alpha_{1,\text{LNA}} A_{\text{in}} k_{\text{TX}} + \frac{3}{4}(2r+3r^3)\alpha_{3,\text{LNA}} A^3_{\text{in}} k_{\text{TX}}, \tag{41}$$

$$C_5 = \frac{3}{4} r\alpha_{3,\text{LNA}} A^3_{\text{in}}, \tag{42}$$

$$C_6 = \frac{3}{4} r^2\alpha_{3,\text{LNA}} A^3_{\text{in}}. \tag{43}$$

The parameter r is the amplitude ratio of the leakage to the target echo signal, which can also be related to the power ratio of the leakage to the echo signal as

$$r = \frac{G_L}{G_R} = \left(\frac{P_{\text{leak}}}{P_{\text{echo}}}\right)^{\frac{1}{2}}. \tag{44}$$

The leakage signal, according to (38), tends to push the LNA more into the gain compression. Furthermore, as can be inferred from (37), the leakage introduces new undesired spectral components in the LNA output which will be translated to the IF band. The parameter A_{in} in (38)–(43) denotes amplitude of the echo signal at the LNA input. The total input power of the LNA, including the echo and leakage signals, can be estimated as $P_{\text{in,LNA}} \propto (1+r^2)A^2_{\text{in}}$. The harmonics level $k_{\text{RX}} = C_2/C_1$ can be derived as

$$k_{\text{RX}} \approx \left[\frac{1+r^2-\beta\left(3+2\,r^2\right)\frac{P_{\text{in,LNA}}}{P_{\text{1dB,LNA}}}}{1+r^2-\beta\left(1+2r^2\right)\frac{P_{\text{in,LNA}}}{P_{\text{1dB,LNA}}}}\right] A_{\text{RX}} k_{\text{TX}}. \tag{45}$$

The IF signal can be derived by mixing the LNA output signal (37) with the multiplier output signal (9), which after

[8]It can be shown that if $X = \cos(nx) + k\cos[(n\pm 1)x]$ where $k^2 \ll 1$, then $X^3 \approx (3/4)\cos(nx) + (9k/4)\cos[(n\pm 1)x] + (1/4)\cos(3nx) + (3k/4)\cos[(3n\pm 1)x]$.

[9]It can be shown that if $X = \cos(nx) + k\cos[(n\pm 1)x]$ and $Y = \cos(ny) + k\cos[(n\pm 1)y]$ where $k^2 \ll 1$, then $X^2Y \approx (1/2)\cos(ny) + (k/2)\cos[(n\pm 1)y] + (1/4)\cos(2nx\pm ny) + (k/4)\cos[2nx\pm(n\pm 1)y] + (k/2)\cos[(2n\pm 1)x\pm ny] + k\cos(ny\pm x)$.

[10]In these derivations, it is assumed that $k^2_{\text{TX}} \ll 1$ which is valid in most practical conditions.

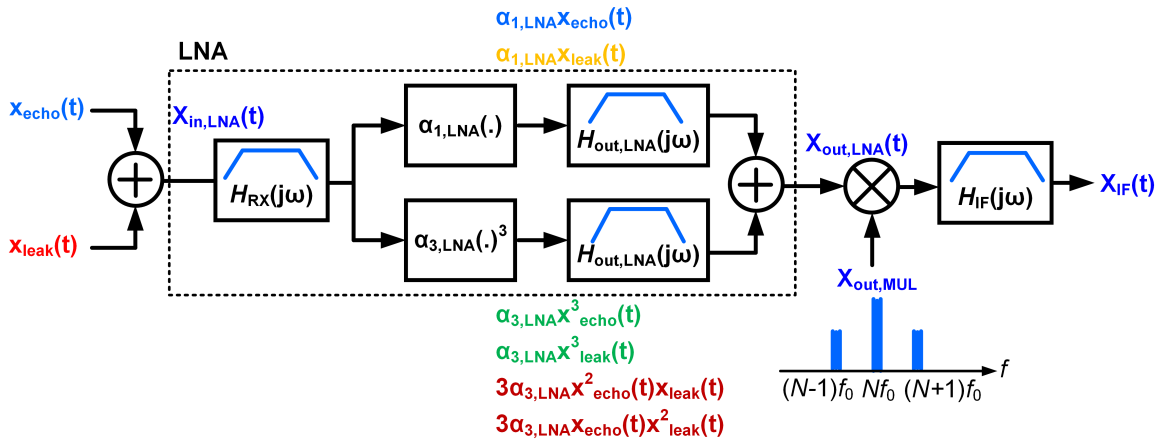

Fig. 5. RX nonlinear system model used to evaluate leakage signal effects.

considering the IF BPF, can be written as

$$\begin{aligned} x_{\rm IF}(t) \approx a_{\rm IF}[&C_1\cos[N\Psi_1(t)] + C_2 k_{\rm ref}\cos[(N\pm 1)\Psi_1(t)] \\ &+ C_3\cos[N\Psi_2(t)] + C_4 k_{\rm ref}\cos[(N\pm 1)\Psi_2(t)] \\ &+ C_5\cos[N\Psi_3(t)] + C_6\cos[N\Psi_4(t)]], \end{aligned} \tag{46}$$

where $\Psi_1(t)$ is defined in (29) and $\Psi_{2,3,4}(t)$ are given by

$$\Psi_2(t) = \Phi(t) - \Phi(t-\tau_L), \tag{47}$$

$$\Psi_3(t) = \Phi(t) - 2\Phi(t-\tau_R) + \Phi(t-\tau_L), \tag{48}$$

$$\Psi_4(t) = \Phi(t) + \Phi(t-\tau_R) - 2\Phi(t-\tau_L). \tag{49}$$

The first and second terms in (46) indicate the presence of spurs at $f_{\rm IF1} = NS\tau_R$ and $f_{\rm IF2,3} = (N\pm 1)S\tau_R$. Similarly, the following three spurs are generated by the third and fourth terms of (46)

$$f_{\rm IF4} = NS\tau_L, \tag{50}$$

$$f_{\rm IF5} = (N+1)S\tau_L, \tag{51}$$

$$f_{\rm IF6} = (N-1)S\tau_L, \tag{52}$$

The last two terms in (46) lead to two spurs at

$$f_{\rm IF7} = NS|2\tau_R - \tau_L|, \tag{53}$$

$$f_{\rm IF8} = NS|\tau_R - 2\tau_L|. \tag{54}$$

The relative magnitudes of these components can be derived using (38)–(44) and (46). The IF BPF can also attenuate some of the undesired components when they are located out of its passband $f_{\rm IF,min} \le f \le f_{\rm IF,max}$. A typical IF spectrum is shown in Fig. 4(b). The frequency spacing between the desired component $f_{\rm IF1}$ and other undesired components is dependent on the target range and the multiplication factor of the frequency multiplier. For typical ranges, $\tau_L \ll \tau_R$ (τ_L is an electrical delay while τ_R is the signal round trip between the radar and target), and the leakage effect can be negligible if its amplitude is not such high that saturates the LNA. For short-range targets, however, τ_L can be close to τ_R, and can mask the target echo if the leakage signal is large. The spectral components $f_{\rm IF2,3}$ can be too close to the desired component when the frequency multiplication factor N is large

$$\frac{f_{\rm IF2,3}}{f_{\rm IF1}} = 1 \pm \frac{1}{N}. \tag{55}$$

The spur level can be derived using (24), (45), and (46) as

$$k_{\rm IF} \approx \left[\frac{1+r^2-\beta\left(3+2r^2\right)\frac{P_{\rm in,LNA}}{P_{\rm 1dB,LNA}}}{1+r^2-\beta\left(1+2r^2\right)\frac{P_{\rm in,LNA}}{P_{\rm 1dB,LNA}}}\right]\left[\frac{1-3\beta\frac{P_{\rm in,PA}}{P_{\rm 1dB,PA}}}{1-\beta\frac{P_{\rm in,PA}}{P_{\rm 1dB,PA}}}\right] \times A_{\rm RX}A_{\rm TX}k_{\rm ref}^2. \tag{56}$$

This includes reference harmonic levels, relative leakage signal magnitude, nonlinearities of the PA and LNA, as well as limited bandwidth of the TX and RX. In the condition that the PA and LNA are operated in their linear power range ($P_{\rm in,PA} \ll P_{\rm 1dB,PA}$ and $P_{\rm in,LNA} \ll P_{\rm 1dB,LNA}$), the spurs level in the IF is derived as

$$k_{\rm IF} \approx A_{\rm RX}A_{\rm TX}k_{\rm ref}^2. \tag{57}$$

This indicates that to achieve a specific spurs level in the IF band, e.g., −80 dB, neglecting harmonics attenuation by the TX and RX ($A_{\rm TX} \approx A_{\rm RX} \approx 1$), the required HRR of the frequency multiplier is 40 dBc. If TX and RX can provide 10 dB harmonic attenuation ($A_{\rm TX} = A_{\rm RX} = 10$ dB), the required HRR will be 30 dBc, which is more practical in mm-wave bands. It is straightforward to show that both the first and second terms in the brackets of (56) are always smaller than 1, and decrease by increasing $P_{\rm in,LNA}$ or $P_{\rm in,PA}$. *Therefore, the PA and LNA nonlinearities tend to reduce the harmonics levels.* For example, if the LNA and PA are operated at their $P_{\rm 1dB}$, each reduces $k_{\rm IF}$ by 2.5 dB. Furthermore, the first term of (56) is a function of r, which for $P_{\rm in,LNA} = P_{\rm 1dB,LNA}$, if r is varied from zero to a large number, it will change from $(1-3\beta)/(1-\beta)$ to 1 (i.e., ≈2.5 dB). Therefore, impact of the leakage signal on *this* IF spur is not significant. However, it will be shown shortly that the leakage signal can generate other IF spurs which whose amplitude is significantly dependent on the leakage signal power.

The spectral components $f_{\rm IF4,5,6}$ can be normalized to the main $f_{\rm IF1}$ component frequency as

$$\frac{f_{\rm IF4}}{f_{\rm IF1}} = \frac{\tau_L}{\tau_R}, \tag{58}$$

$$\frac{f_{\rm IF5,6}}{f_{\rm IF1}} = \left(1 \pm \frac{1}{N}\right)\frac{\tau_L}{\tau_R}, \tag{59}$$

which are usually located at low frequencies in the practical $\tau_L \ll \tau_R$ condition. The spectral component f_{IF4} have a relative amplitude of C_3/C_1 with respect to the main IF component, while for $f_{\mathrm{IF5,6}}$ components this is given by $(C_4/C_1)k_{\mathrm{ref}}$. However, these spurs are usually located at low frequencies and can be significantly suppressed by the lower-band attenuation of the IF BPF $A_{\mathrm{IF,L}}$. Therefore, the spurs levels after passing through the IF filter can be derived as

$$k_{\mathrm{IF,II}} = \left[\frac{1+r^2-\beta\left(2+r^2\right)\frac{P_{\mathrm{in,LNA}}}{P_{\mathrm{1dB,LNA}}}}{1+r^2-\beta\left(1+2r^2\right)\frac{P_{\mathrm{in,LNA}}}{P_{\mathrm{1dB,LNA}}}}\right] r A_{\mathrm{IF,L}}, \tag{60}$$

$$k_{\mathrm{IF,III}} = \left[\frac{1+r^2-\beta\left(2+3\ r^2\right)\frac{P_{\mathrm{in,LNA}}}{P_{\mathrm{1dB,LNA}}}}{1+r^2-\beta\left(3+2r^2\right)\frac{P_{\mathrm{in,LNA}}}{P_{\mathrm{1dB,LNA}}}}\right] r k_{\mathrm{IF}} A_{\mathrm{IF,L}}. \tag{61}$$

The attenuation $A_{\mathrm{IF,L}}$ is practically realized using an HPF with very low cut-off frequency [8], [9]. If τ_L and τ_R are comparable, these components can be close to $f_{\mathrm{IF1,2,3}}$.

The spectral component f_{IF7} can be normalized to f_{IF1} as

$$\frac{f_{\mathrm{IF7}}}{f_{\mathrm{IF1}}} = \left|2-\frac{\tau_L}{\tau_R}\right|, \tag{62}$$

which is close to $2f_{\mathrm{IF1}}$ for small τ_L. The relative magnitude of f_{IF7} to f_{IF1} is $|C_5|/C_1$. Furthermore, in the condition that f_{IF7} is higher than the upper cut-off frequency of the IF BPF (i.e., $f_{\mathrm{IF7}} > f_{\mathrm{IF,max}}$), it will be attenuated by $A_{\mathrm{IF,H}}$ (see Fig. 2). Therefore, the spur level is $k_{\mathrm{IF,IV}} = (|C_5|/C_1)A_{\mathrm{IF,H}}$, which can be derived as

$$k_{\mathrm{IF,IV}} \approx \left[\frac{\beta r\frac{P_{\mathrm{in,LNA}}}{P_{\mathrm{1dB,LNA}}}}{1+r^2-\beta\left(1+2r^2\right)\frac{P_{\mathrm{in,LNA}}}{P_{\mathrm{1dB,LNA}}}}\right] A_{\mathrm{IF,H}}. \tag{63}$$

If f_{IF7} is inside the IF BPF band (i.e., $f_{\mathrm{IF7}} < f_{\mathrm{IF,max}}$), $A_{\mathrm{IF,H}} = 1$ should be assumed. In this case, the spur f_{IF7} can be collocated with another target range within R_{min} to R_{max} which cannot be suppressed by the IF BPF. The spectral component f_{IF7} which is a result of interaction between the TX-to-RX leakage and the LNA nonlinearity is independent of the reference harmonics and can have either a higher or lower magnitude compared to the spurs $f_{\mathrm{IF2,3}}$. This should be mitigated by increasing attenuation of the IF BPF in the upper stop-band (if $f_{\mathrm{IF7}} > f_{\mathrm{IF,max}}$), suppressing the leakage signal, or decreasing the LNA nonlinearity [see (63)].

The spectral component f_{IF8} can be normalized to f_{IF1} as

$$\frac{f_{\mathrm{IF8}}}{f_{\mathrm{IF1}}} = \left|1-2\frac{\tau_L}{\tau_R}\right|, \tag{64}$$

which is close to f_{IF1} for small τ_L. The relative magnitude of f_{IF8} to f_{IF1} is given by $k_{\mathrm{IF,V}} = |C_6|/C_1$ which can be derived as

$$k_{\mathrm{IF,V}} \approx \left[\frac{\beta r^2\frac{P_{\mathrm{in,LNA}}}{P_{\mathrm{1dB,LNA}}}}{1+r^2-\beta\left(1+2r^2\right)\frac{P_{\mathrm{in,LNA}}}{P_{\mathrm{1dB,LNA}}}}\right]. \tag{65}$$

This can also be higher or lower than k_{IF} and should be mitigated by reducing the leakage signal and the LNA nonlinearity. The component f_{IF8} is close to the main component in the IF band and unlike the component f_{IF7} cannot be easily suppressed by the IF BPF [see Fig. 4(b)]. A summary of the IF spurs' frequency and relative amplitude (Fig. 4) is presented in Table I.

TABLE I
SUMMARY OF THE IF SPURS' FREQUENCY AND AMPLITUDE

Spur Component	Frequency	Amplitude
f_{IF1}	$f_{\mathrm{IF1}} = NS\tau_R$	1
f_{IF2}	$f_{\mathrm{IF2}} = (N+1)S\tau_R$	k_{IF}
f_{IF3}	$f_{\mathrm{IF3}} = (N-1)S\tau_R$	k_{IF}
f_{IF4}	$f_{\mathrm{IF4}} = NS\tau_L$	$k_{\mathrm{IF,II}}$
f_{IF5}	$f_{\mathrm{IF5}} = (N+1)S\tau_L$	$k_{\mathrm{IF,III}}$
f_{IF6}	$f_{\mathrm{IF6}} = (N-1)S\tau_L$	$k_{\mathrm{IF,III}}$
f_{IF7}	$f_{\mathrm{IF7}} = NS\lvert 2\tau_R - \tau_L\rvert$	$k_{\mathrm{IF,IV}}$
f_{IF8}	$f_{\mathrm{IF8}} = NS\lvert \tau_R - 2\tau_L\rvert$	$k_{\mathrm{IF,V}}$

In Fig. 6, the spurs level k_{IF}, $k_{\mathrm{IF,II}}$, $k_{\mathrm{IF,III}}$, $k_{\mathrm{IF,IV}}$, and $k_{\mathrm{IF,V}}$ are shown versus the relative leakage signal power, $10\log_{10}(P_{\mathrm{leak}}/P_{\mathrm{echo}})$. It is assumed that $k_{\mathrm{ref}} = 0.1$, $A_{\mathrm{TX}} = A_{\mathrm{RX}} = 1$, and the PA and LNA are operated at their P_{1dB}. In Fig. 6(a), where $A_{\mathrm{IF,L}} = A_{\mathrm{IF,H}} = -20$ dB, at low relative leakage power levels the maximum spur level is k_{IF} which is generated by the harmonics of the frequency multiplier. However, for relative leakage power levels roughly ≥ -20 dB, the spur level $k_{\mathrm{IF,II}}$ will become greater, which is a result of interaction between the leakage signal and the LNA nonlinearity. In Fig. 6(b), the IF filter features higher stop-band attenuation $A_{\mathrm{IF,L}} = A_{\mathrm{IF,H}} = -40$ dB. In this case, the spurs level $k_{\mathrm{IF,II}}$, $k_{\mathrm{IF,III}}$, and $k_{\mathrm{IF,IV}}$ are attenuated by 20 dB. The k_{IF} is the largest spur at low leakage power levels, $k_{\mathrm{IF,V}}$ dominates in the medium leakage power ranges around 0 dB, while $k_{\mathrm{IF,II}}$ is the dominant spur in the large leakage power levels. It can be concluded that a low reference harmonics level k_{ref} is a necessary but not sufficient condition to achieve a low IF spurs level. The IF filter should also provide high stop-band attenuation ($A_{\mathrm{IF,L}}$ and $A_{\mathrm{IF,H}}$).

In Fig. 7, the maximum spur level is shown versus the relative leakage signal power for four sets of system parameters. It is assumed that $A_{\mathrm{TX}} = A_{\mathrm{RX}} = 1$. The PA and LNA are driven in their P_{1dB}. It is noted that a low k_{ref} leads to low IF spurs when the leakage signal is small. In the presence of strong leakage signals, however, high attenuation should be provided by the IF filter to suppress the extra spurs.

The developed theory can provide design guidelines for the required stop-band attenuation of the IF BPF for a given relative leakage power. Using (56) and (60), the required $A_{\mathrm{IF,L}}$ to meet the condition $k_{\mathrm{IF,II}} < k_{\mathrm{IF}}$ can be derived. Moreover, the required $A_{\mathrm{IF,H}}$ can be derived using (56) and (63) to satisfy $k_{\mathrm{IF,IV}} < k_{\mathrm{IF}}$.

C. Radar Dynamic Range

The radar dynamic range (DR) can be used as a practical measure of the radar performance. It can be derived as the difference between the RX signal power and its noise floor ($\mathrm{DR_{noise}}$) when noise is dominant or as the difference between the signal power and the maximum spur level ($\mathrm{DR_{spur}}$) when the spur power is higher than the noise floor. The radar DR

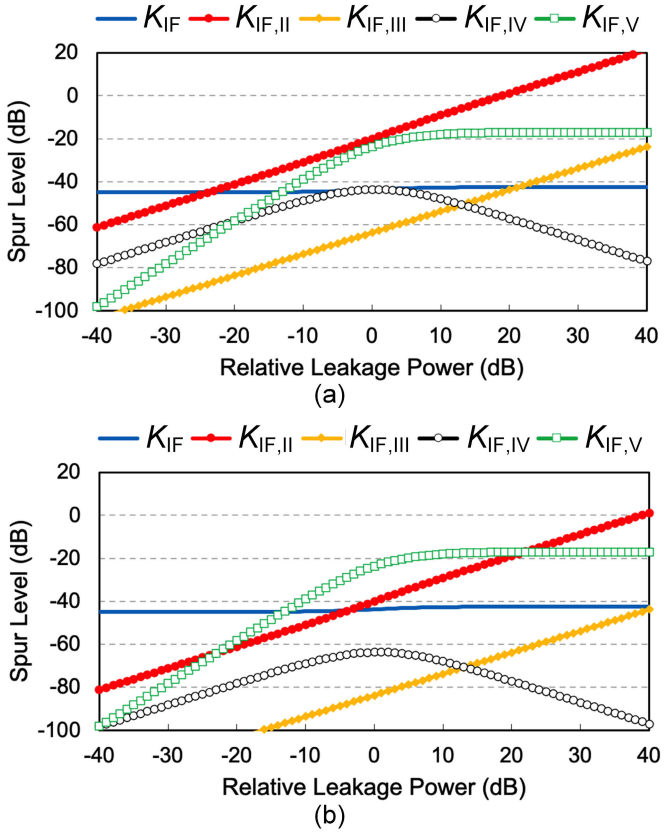

Fig. 6. Spurs level versus the relative leakage signal power. (a) $A_{\mathrm{IF,L}} = A_{\mathrm{IF,H}} = -20\,\mathrm{dB}$, (b) $A_{\mathrm{IF,L}} = A_{\mathrm{IF,H}} = -40\,\mathrm{dB}$. It is assumed that $k_{\mathrm{ref}} = -20\,\mathrm{dB}$ ($= 0.1$) and $A_{\mathrm{TX}} = A_{\mathrm{RX}} = 0\,\mathrm{dB}$. The PA and LNA are operated at their $P_{1\mathrm{dB}}$.

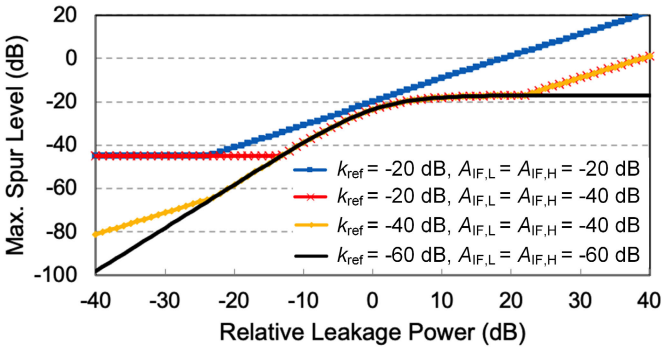

Fig. 7. Maximum spurs level versus the relative leakage signal power. It is assumed that $A_{\mathrm{TX}} = A_{\mathrm{RX}} = 0\,\mathrm{dB}$. The PA and LNA are operated at their $P_{1\mathrm{dB}}$.

can be maximized by limiting the largest spur below the noise floor, i.e., $\mathrm{DR}_{\mathrm{spur}} = \mathrm{DR}_{\mathrm{noise}}$, which can be derived as

$$-20\log_{10}(k_{\mathrm{IF,max}}) = P_{\mathrm{RX,max}} + 174 - NF - 10\log_{10}(B_n), \tag{66}$$

where $k_{\mathrm{IF,max}}$ is the maximum spur level in the IF band, $P_{\mathrm{RX,max}}$ is the maximum input power of the RX (can be considered as $P_{1\mathrm{dB,LNA}}$), NF is the RX noise figure, and B_n is the effective noise bandwidth ($B_n = 1/T_c$). This condition can be used to determine acceptable harmonics level at output of the frequency multiplier, the TX-to-RX leakage power, and nonlinearity of the PA and LNA.

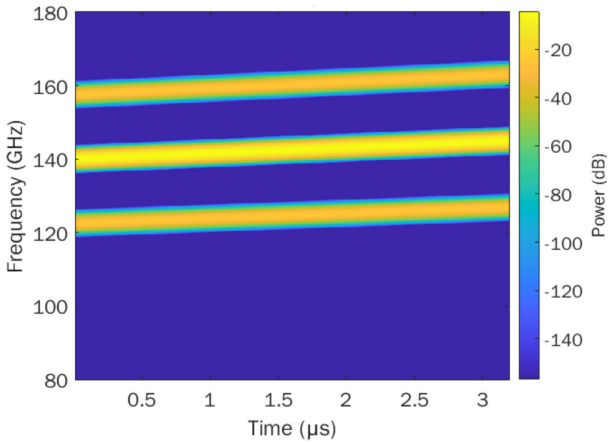

Fig. 8. Spectrogram of the 140-GHz chirp signal with 5 GHz bandwidth. The $\times 8$ frequency multiplier includes harmonics at $(N \pm 1) f_{\mathrm{ref}}$ with $-20\,\mathrm{dBc}$ power level ($k_{\mathrm{ref}} = 0.1$).

TABLE II

COMPARISON OF THE THEORETICAL AND SIMULATION RESULTS FOR IF SPURS LEVEL k_{IF}. THE SYSTEM PARAMETERS ARE $k_{\mathrm{Ref}} = 0.1$, $P_{\mathrm{in,PA}} = P_{1\mathrm{dB,PA}}$, $P_{\mathrm{in,LNA}} = P_{1\mathrm{dB,LNA}}$

Source of Nonlinearity	Theory	Simulation
Multiplier	−40.0 dBc	−40.3 dBc
Multiplier, PA	−42.5 dBc	−42.6 dBc
Multiplier, LNA	−42.5 dBc	−42.6 dBc
Multiplier, PA, LNA	−45.0 dBc	−44.6 dBc
Multiplier, PA, LNA, Leakage (−20 dB)	−44.9 dBc	−45.2 dBc
Multiplier, PA, LNA, Leakage (−10 dB)	−44.7 dBc	−44.2 dBc
Multiplier, PA, LNA, Leakage (0 dB)	−43.7 dBc	−43.9 dBc
Multiplier, PA, LNA, Leakage (+10 dB)	−42.7 dBc	−44.7 dBc
Multiplier, PA, LNA, Leakage (+20 dB)	−42.5 dBc	−45.5 dBc

IV. SIMULATIONS AND DISCUSSIONS

A. Simulation Setup

The developed nonlinear system model for FMCW radars is verified through Keysight Advanced Design System (ADS) and MATLAB simulations. The TX and RX circuits including their nonlinearity and bandwidth limitation are modeled in the ADS and MATLAB. The reference signal is a 17.5-GHz chirp waveform with 625 MHz bandwidth and 3.2 μs duration. The $\times 8$ frequency multiplier transforms the reference signal to a 140-GHz chirp with 5 GHz bandwidth, while it includes two harmonics at $(N \pm 1) f_{\mathrm{ref}}$. Spectrogram of the chirp signal is shown in Fig. 8, where the harmonics level is $-20\,\mathrm{dBc}$ ($k_{\mathrm{ref}} = 0.1$). A high level of harmonics is intentionally used to investigate its effects on the radar performance. It is assumed that $A_{\mathrm{TX}} = A_{\mathrm{RX}} = 1$. The down-converted signal at IF is sampled, is passed through a digital filter and, subsequently, the FFT processing is performed to extract the spectrum, range, and Doppler information.

B. Radar IF Spectrum

The FMCW radar with the developed nonlinear model is considered for detecting a target located at the range of $R = 10\,\mathrm{m}$. The radar IF spectrum for different sources of

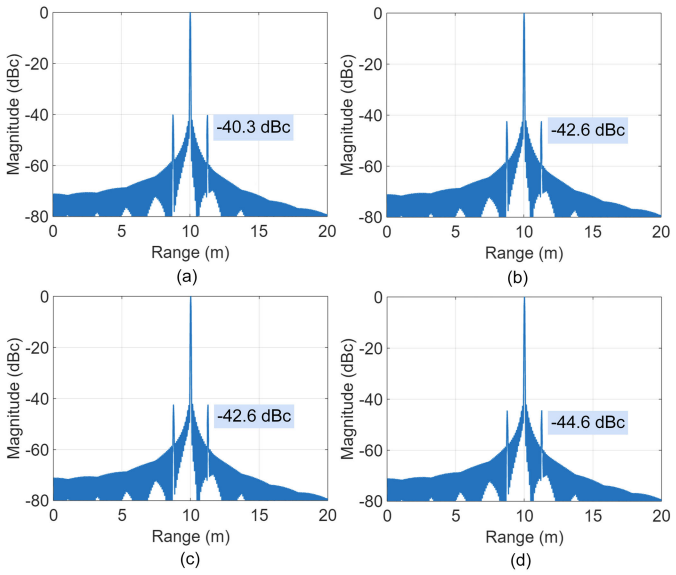

Fig. 9. Impact of circuit nonlinearities on radar IF spectrum. (a) Frequency multiplier, (b) frequency multiplier and PA, (c) frequency multiplier and LNA, (d) frequency multiplier, PA, and LNA. The $\times 8$ frequency multiplier includes harmonics at $(N \pm 1) f_{\text{ref}}$ with -20 dBc power level ($k_{\text{ref}} = 0.1$). The PA and LNA are operated at their $P_{1\text{dB}}$.

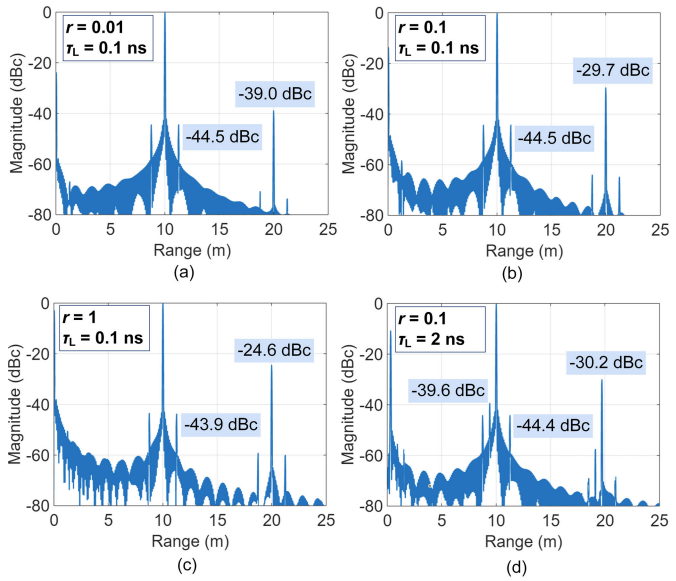

Fig. 10. Impact of the TX-to-RX leakage on radar IF spectrum. $r = G_L/G_R$ denotes relative amplitude of the leakage signal to the target echo and τ_L is the leakage signal delay with respect to the TX signal. The $\times 8$ frequency multiplier has -20 dBc harmonics level. The PA and LNA are operated at their $P_{1\text{dB}}$.

nonlinearity included in the model is shown in Fig. 9. The IF frequency is mapped to the target range. The IF BPF and the window effect are not applied to enable a fair comparison between theory and simulations. The main spectral component f_{IF1} corresponds to the range of $R = 10$ m, while the spectral components $f_{\text{IF2,3}}$ are related to the ranges $(1 \pm 1/N)R = 8.75$ m, 11.25 m. In Fig. 9(a), only the frequency multiplier harmonics with $k_{\text{ref}} = 0.1$ are included. The IF harmonics level reads -40.3 dBc, which is close to the theoretical value of $20 \log_{10}(k_{\text{ref}}^2) = -40$ dBc. The effect of frequency multiplier

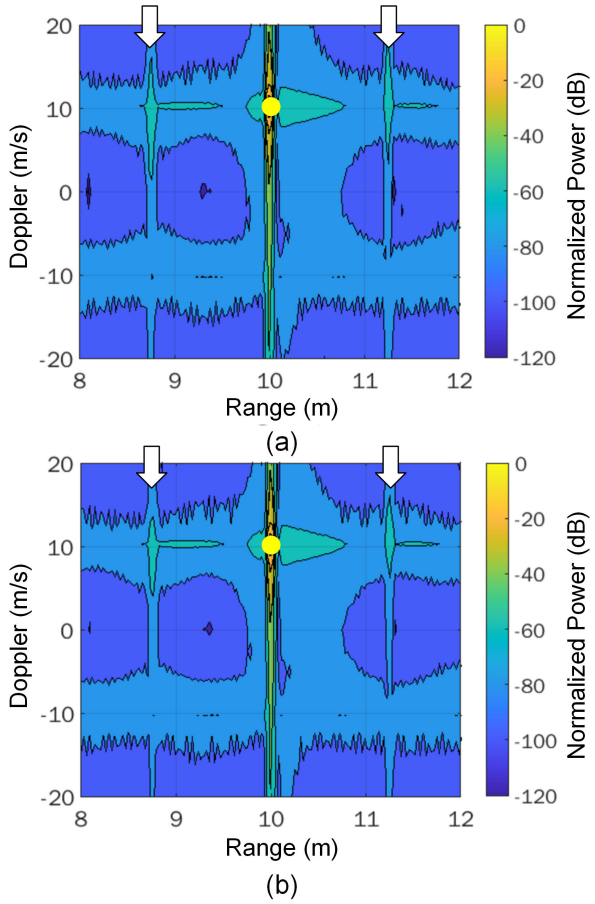

Fig. 11. Impact of circuit nonlinearities on the Range-Doppler diagram. (a) Frequency multiplier, (b) frequency multiplier, PA, and LNA. The main target highlighted by the yellow circle is located at $(R, D) = (10\,\text{m}, 10\,\text{m/s})$, while other high-power areas corresponding to the spurs are indicated by arrows.

and PA nonlinearity is shown in Fig. 9(b), while Fig. 9(c) indicates the effect of the frequency multiplier and LNA nonlinearity, and Fig. 9(d) demonstrates the effect of the frequency multiplier, PA, and LNA nonlinearities. The PA and LNA are operated at their $P_{1\text{dB}}$. Simulation and theoretical results, derived using (30), are compared in Table II. The difference between the theory and simulation results is ≤ 0.5 dB up to the relative leakage power of 0 dB. The discrepancy however increases to $\sim$2–3 dB for higher relative leakage power levels. This is due to the approximations used in the theory and the finite resolution of numerical simulations. Therefore, the developed model can provide fairly accurate results without using time-consuming system simulations.

The radar IF spectrum in the presence of TX-to-RX leakage is shown in Fig. 10. The relative leakage signal amplitude is increased from $r = 0.01$ in Fig. 10(a) to $r = 0.1$ and $r = 1$ in Fig. 10(b) and Fig. 10(c), respectively. The leakage signal delay $\tau_L = 0.1$ ns is much smaller than the target echo delay. Therefore, *in practice*, the low-frequency spectral components associated with the leakage will be highly suppressed by the IF BPF. Other than the two spectral components $f_{\text{IF2,3}}$, another spur is also observed at f_{IF7}. The relative amplitude of this component, e.g., in Fig. 10(c), is -24.6 dBc. This is

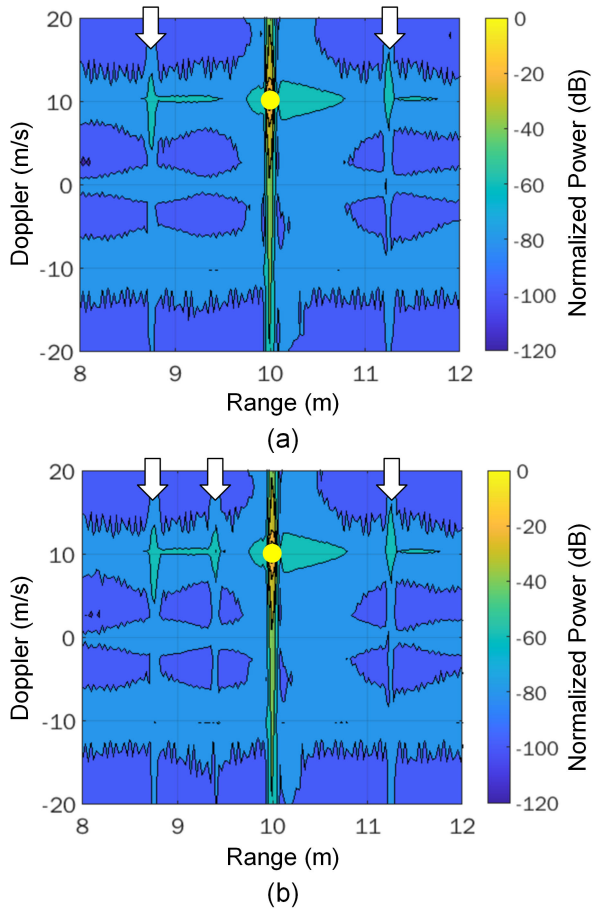

Fig. 12. Impact of the TX-to-RX leakage on the Range-Doppler diagram. (a) $\tau_L = 0.1\,\text{ns}$, $r = 0.1$, (b) $\tau_L = 2\,\text{ns}$, $r = 0.1$. All system nonlinearities are included. The main target highlighted by the yellow circle is located at $(R, D) = (10\,\text{m}, 10\,\text{m/s})$, while other high-power areas corresponding to the spurs are indicated by arrows.

close to the theoretical value of $20\log_{10}(k_{\text{IF,III}}) = -23.6\,\text{dBc}$. In Fig. 10(d), the leakage signal delay is increased to $\tau_L = 2\,\text{ns}$ in order to observe the spur f_{IF8}. This is close to the main component and its magnitude is larger than that of the components $f_{\text{IF2,3}}$. The leakage signal should therefore be attenuated through increasing the TX-RX isolation to achieve low spectral components at $f_{\text{IF7,8}}$.

C. Radar Range-Doppler Diagram

The radar Range-Doppler diagram can provide insights about the effects of circuit nonlinearities on the features of detected target(s). It is assumed that the radar operates over 1–80 m target range and $\pm 50\,\text{m/s}$ maximum target velocity. The target initial range and velocity are respectively 10 m and 10 m/s. The IF BPF provides high out-of-band attenuation over the bandwidth $f_{\text{IF,min}}$ and $f_{\text{IF,max}}$. The transmitted signal is composed of 128 chirps.

In Fig. 11(a), the Range-Doppler diagram is shown when only the frequency multiplier harmonics are included in the radar nonlinear model. The maximum power level is read around the point $(R, D) = (10\,\text{m}, 10\,\text{m/s})$ which indicates that the radar can provide high detection probability for the target. However, the relatively high power levels around $(8.75\,\text{m}, 10\,\text{m/s})$ and $(11.25\,\text{m}, 10\,\text{m/s})$ (shown in light green) indicate a probability of false alarm close to these points. In Fig. 11(b) where the PA and LNA nonlinearity are also included, the light green areas around $(8.75\,\text{m}, 10\,\text{m/s})$ and $(11.25\,\text{m}, 10\,\text{m/s})$ have been shrunk. This indicates a lower false alarm probability as a result of the reduced IF band spurs level (by $\approx 5\,\text{dB}$). In Fig. 12, effects of the TX-to-RX leakage are illustrated when all of the system nonlinearities are included. For the leakage signal delay of $\tau_L = 2\,\text{ns}$, a light green area appears between 9–10 m close to the main target area. This is a result of the spectral component f_{IF8} which can increase the false alarm probability.

V. Conclusion

We presented a nonlinear system model for millimeter-wave frequency-modulated continuous-wave (FMCW) radar system-on-chips (SoC). The model included harmonics of the frequency multiplier, nonlinearity of the power amplifier (PA), low-noise amplifier (LNA), and the switching operation of the mixer, as well as impact of the TX-to-RX leakage signal. The developed model can predict the frequency and amplitude of spurs in the radar IF spectrum prior to the circuit design.

References

[1] J. Hatch, A. Topak, R. Schnabel, T. Zwick, R. Weigel, and C. Waldschmidt, "Millimeter-wave technology for automotive radar sensors in the 77 GHz frequency band," *IEEE Trans. Microw. Theory Techn.*, vol. 60, no. 3, pp. 845–860, Mar. 2012.

[2] C. Waldschmidt, J. Hasch, and W. Menzel, "Automotive radar—From first efforts to future systems," *IEEE J. Microw.*, vol. 1, no. 1, pp. 135–148, Jan. 2021.

[3] S. Trotta et al., "SOLI: A tiny device for a new human machine interface," in *IEEE Int. Solid-State Circuits Conf. (ISSCC) Dig. Tech. Papers*, Feb. 2021, pp. 42–44.

[4] Y. Li, C. Gu, and J. Mao, "4-D gesture sensing using reconfigurable virtual array based on a 60-GHz FMCW MIMO radar sensor," *IEEE Trans. Microw. Theory Techn.*, vol. 70, no. 7, pp. 3652–3665, Jul. 2022.

[5] A. Visweswaran et al., "A 28-nm-CMOS based 145-GHz FMCW radar: System, circuits, and characterization," *IEEE J. Solid-State Circuits*, vol. 56, no. 7, pp. 1975–1993, Jul. 2021.

[6] M. Kucharaski, W. A. Ahmad, H. J. Ng, and D. Kissinger, "Monostatic and bistatic G-band BiCMOS radar transceivers with on-chip antennas and tunable TX-to-RX leakage cancellation," *IEEE J. Solid-State Circuits*, vol. 56, no. 3, pp. 899–913, Mar. 2021.

[7] S. M. H. Naghavi, S. Seyedabbaszadehesfahlani, F. Khoeini, A. Cathelin, and E. Afshari, "A 250 GHz autodyne FMCW radar in 55 nm BiCMOS with micrometer range resolution," in *IEEE Int. Solid-State Circuits Conf. (ISSCC) Dig. Tech. Papers*, Feb. 2021, pp. 320–322.

[8] A. Kankuppe et al., "A 67 mW D-band FMCW I/Q radar receiver with an N-path spillover notch filter in 28 nm CMOS," in *Proc. IEEE 47th Eur. Solid State Circuits Conf. (ESSCIRC)*, Sep. 2021, pp. 471–474.

[9] A. Kankuppe, S. Park, P. T. Renukaswamy, P. Wambacq, and J. Craninckx, "A wideband 62-mW 60-GHz FMCW radar in 28-nm CMOS," *IEEE Trans. Microw. Theory Techn.*, vol. 69, no. 6, pp. 2921–2935, Jun. 2021.

[10] K. Statnikov, E. Ojefors, J. Grzyb, P. Chevalier, and U. R. Pfeiffer, "A 0.32 THz FMCW radar system based on low-cost lens-integrated SiGe HBT front-ends," in *Proc. ESSCIRC*, Sep. 2013, pp. 81–84.

[11] J. Grzyb, K. Statnikov, N. Sarmah, B. Heinemann, and U. R. Pfeiffer, "A 210–270-GHz circularly polarized FMCW radar with a single-lens-coupled SiGe HBT chip," *IEEE Trans. Terahertz Sci. Technol.*, vol. 6, no. 6, pp. 771–783, Nov. 2016.

[12] T. Jaeschke, C. Bredendiek, S. Küppers, and N. Pohl, "High-precision D-band FMCW-radar sensor based on a wideband SiGe-transceiver MMIC," *IEEE Trans. Microw. Theory Techn.*, vol. 62, no. 12, pp. 3582–3597, Dec. 2014.

[13] S. Thomas, C. Bredendiek, and N. Pohl, "A SiGe-based 240-GHz FMCW radar system for high-resolution measurements," *IEEE Trans. Microw. Theory Techn.*, vol. 67, no. 11, pp. 4599–4609, Nov. 2019.

[14] M. Hitzler et al., "Ultracompact 160-GHz FMCW radar MMIC with fully integrated offset synthesizer," *IEEE Trans. Microw. Theory Techn.*, vol. 65, no. 5, pp. 1682–1691, May 2017.

[15] V. Giannini et al., "A 192-virtual-receiver 77/79 GHz GMSK code-domain MIMO radar system-on-chip," in *IEEE Int. Solid-State Circuits Conf. (ISSCC) Dig. Tech. Papers*, Feb. 2019, pp. 164–166.

[16] A. Zandieh, S. Bonen, M. S. Dadash, M. J. Gong, J. Hasch, and S. P. Voinigescu, "155 GHz FMCW and stepped-frequency carrier OFDM radar sensor transceiver IC featuring a PLL with <30 ns settling time and 40 fs_{rms} jitter," *IEEE Trans. Microw. Theory Techn.*, vol. 69, no. 11, pp. 4908–4924, Nov. 2021.

[17] A. Mostajeran, A. Cathelin, and E. Afshari, "A 170-GHz fully integrated single-chip FMCW imaging radar with 3-D imaging capability," *IEEE J. Solid-State Circuits*, vol. 52, no. 10, pp. 2721–2734, Oct. 2017.

[18] D. Guermandi et al., "A 79 GHz binary phase-modulated continuous-wave radar transceiver with TX-to-RX spillover cancellation in 28 nm CMOS," in *IEEE Int. Solid-State Circuits Conf. (ISSCC) Dig. Tech. Papers*, Feb. 2015, pp. 1–3.

[19] D. Guermandi et al., "A 79-GHz 2 × 2 MIMO PMCW radar SoC in 28-nm CMOS," *IEEE J. Solid-State Circuits*, vol. 52, no. 10, pp. 2613–2626, Oct. 2017.

[20] A. Medra et al., "An 80 GHz low-noise amplifier resilient to the TX spillover in phase-modulated continuous-wave radars," *IEEE J. Solid-State Circuits*, vol. 51, no. 5, pp. 1141–1153, May 2016.

[21] G. Pyo, C.-Y. Kim, and S. Hong, "Single-antenna FMCW radar CMOS transceiver IC," *IEEE Trans. Microw. Theory Techn.*, vol. 65, no. 3, pp. 945–954, Mar. 2017.

[22] M. Kalantari, W. Li, H. Shirinabadi, A. Fotowat-Ahmady, and C. P. Yue, "A W-band single-antenna FMCW radar transceiver with adaptive leakage cancellation," *IEEE J. Solid-State Circuits*, vol. 56, no. 6, pp. 1655–1667, Jun. 2021.

[23] W. Lee, T. Dinc, and A. Valdes-Garcia, "Multi-mode 60-GHz radar transmitter SoC in 45-nm SOI CMOS," *IEEE J. Solid-State Circuits*, vol. 55, no. 5, pp. 1187–1198, May 2020.

[24] E. Fishler, A. Haimovich, R. Blum, D. Chizhik, L. Cimini, and R. Valenzuela, "MIMO radar: An idea whose time has come," in *Proc. IEEE Radar Conf.* Philadelphia, PA, USA, Mar. 2004, pp. 71–78.

[25] G. Hakobyan and B. Yang, "High-performance automotive radar: A review of signal processing algorithms and modulation schemes," *IEEE Signal Process. Mag.*, vol. 36, no. 5, pp. 32–44, Sep. 2019.

[26] S. M. Patole, M. Torlak, D. Wang, and M. Ali, "Automotive radars: A review of signal processing techniques," *IEEE Signal Process. Mag.*, vol. 34, no. 2, pp. 22–35, Mar. 2017.

[27] A. G. Stove, "Linear FMCW radar techniques," *IEE Proc. F Radar Signal Process.*, vol. 139, no. 5, pp. 343–350, Oct. 1992.

[28] S. Ayhan, S. Scherr, A. Bhutani, B. Fischbach, M. Pauli, and T. Zwick, "Impact of frequency ramp nonlinearity, phase noise, and SNR on FMCW radar accuracy," *IEEE Trans. Microw. Theory Techn.*, vol. 64, no. 10, pp. 3290–3301, Oct. 2016.

[29] M. I. Skolnik, *Introduction to Radar Systems*. 3rd ed. New York, NY, USA: McGraw-Hill, 2002.

[30] B. Razavi, *RF Microelectronics*, 2nd ed. Upper Saddle River, NJ, USA: Prentice-Hall, 2011.

[31] W. Wu, R. B. Staszewski, and J. R. Long, "A 56.4-to-63.4 GHz multi-rate all-digital fractional-N PLL for FMCW radar applications in 65 nm CMOS," *IEEE J. Solid-State Circuits*, vol. 49, no. 5, pp. 1081–1096, May 2014.

[32] D. Cherniak, L. Grimaldi, L. Bertulessi, R. Nonis, C. Samori, and S. Levantino, "A 23-GHz low-phase-noise digital bang-bang PLL for fast triangular and sawtooth chirp modulation," *IEEE J. Solid-State Circuits*, vol. 53, no. 12, pp. 3565–3575, Dec. 2018.

[33] Q. Shi, K. Bunsen, N. Markulic, and J. Craninckx, "A self-calibrated 16-GHz subsampling-PLL-based fast-chirp FMCW modulator with 1.5-GHz bandwidth," *IEEE J. Solid-State Circuits*, vol. 54, no. 12, pp. 3503–3512, Dec. 2019.

[34] P. T. Renukaswamy, N. Markulic, P. Wambacq, and J. Craninckx, "A 12-mW 10-GHz FMCW PLL based on an integrating DAC with 28-kHz RMS-frequency-error for 23-MHz/μs slope and 1.2-GHz chirp-bandwidth," *IEEE J. Solid-State Circuits*, vol. 55, no. 12, pp. 3294–3307, Dec. 2020.

[35] F. Herzel, S. Waldmann, and D. Kissinger, "Numerical jitter minimization for PLL-based FMCW radar systems," *IEEE Trans. Circuits Syst. I, Reg. Papers*, vol. 66, no. 7, pp. 2478–2488, Jul. 2019.

[36] K. Siddiq, M. K. Hobden, S. R. Pennock, and R. J. Watson, "Phase noise in FMCW radar systems," *IEEE Trans. Aerosp. Electron. Syst.*, vol. 55, no. 1, pp. 70–81, Feb. 2019.

[37] A. Ergintav, F. Herzel, G. Fischer, and D. Kissinger, "A study of phase noise and frequency error of a fractional-N PLL in the course of FMCW chirp generation," *IEEE Trans. Circuits Syst. I, Reg. Papers*, vol. 66, no. 5, pp. 1670–1680, May 2019.

[38] F. Herzel, D. Kissinger, and H. J. Ng, "Analysis of ranging precision in an FMCW radar measurement using a phase-locked loop," *IEEE Trans. Circuits Syst., I, Reg. Papers*, vol. 65, no. 2, pp. 783–792, Feb. 2018.

[39] J. Zhang, S. S. Ahmed, and A. Arbabian, "Effects of reference frequency harmonic spurs in FMCW radar systems," in *Proc. IEEE Radar Conf.*, May 2021, pp. 1–6.

[40] R. Nikandish, A. Yousefi, and A. Bozorg, "Impact of circuit nonlinearities on the performance of millimeter-wave FMCW radar-on-chip systems," in *Proc. IEEE Radar Conf.*, Mar. 2022, pp. 1–6.

[41] B. De Muer and M. S. J. Steyaert, "On the analysis of delta-sigma fractional-N frequency synthesizers for high spectral purity," *IEEE Trans. Circuits Syst. II, Analog Digit. Signal Process.*, vol. 50, no. 11, pp. 784–793, Nov. 2003, doi: 10.1109/TCSII.2003.819119.

[42] P. V. Brennan, H. Wang, D. Jiang, and P. M. Radmore, "A new mechanism producing discrete spurious components in fractional-N frequency synthesizers," *IEEE Trans. Circuits Syst. I, Reg. Papers*, vol. 55, no. 5, pp. 1279–1288, Jun. 2008, doi: 10.1109/TCSI.2008.916694.

[43] M. Kucharski, F. Herzel, and D. Kissinger, "Time-domain simulation of quantization noise mixing and charge pump device noise in fractional-N PLLs," in *Proc. IEEE 13th Int. New Circuits Syst. Conf. (NEWCAS)*, Jun. 2015, pp. 1–4, doi: 10.1109/NEWCAS.2015.7182079.

[44] T. Mausolf, F. Herzel, and G. Fischer, "An integrated circuit to reduce phase noise and spurious tones in radar systems," in *Proc. IEEE Nordic Circuits Syst. Conf. (NorCAS)*, Oct. 2022, pp. 1–5, doi: 10.1109/NorCAS57515.2022.9934454.

[45] G. R. Nikandish, R. B. Staszewski, and A. Zhu, "Broadband fully integrated GaN power amplifier with minimum-inductance BPF matching and two-transistor AM-PM compensation," *IEEE Trans. Circuits Syst. I, Reg. Papers*, vol. 67, no. 12, pp. 4211–4223, Dec. 2020.

[46] C. X. Mao, Y. Zhang, X. Y. Zhang, P. Xiao, Y. Wang, and S. Gao, "Filtering antennas: Design methods and recent developments," *IEEE Microw. Mag.*, vol. 22, no. 11, pp. 52–63, Nov. 2021.

[47] M. Bassi et al., "A 39-GHz frequency tripler with >40-dBc harmonic rejection for 5G communication systems in 28-nm bulk CMOS," *IEEE Solid-State Circuits Lett.*, vol. 2, no. 9, pp. 107–110, Sep. 2019.

[48] J. Zhang, Y. Peng, H. Liu, Y. Wu, C. Zhao, and K. Kang, "A 21.7-to-41.7-GHz injection-locked LO generation with a narrowband low-frequency input for multiband 5G communications," *IEEE Trans. Microw. Theory Techn.*, vol. 68, no. 1, pp. 170–183, Jan. 2020.

[49] M. A. Shehata, V. Roy, J. Breslin, H. Shanan, M. Keaveney, and R. B. Staszewski, "A 32–42-GHz RTWO-based frequency quadrupler achieving >37 dBc harmonic rejection in 22-nm FD-SOI," *IEEE Solid-State Circuits Lett.*, vol. 4, pp. 72–75, 2021.

[50] K.-H. Nam, N.-P. Hong, and J.-S. Park, "A 16-times frequency multiplier for 5G synthesizer," *IEEE Trans. Microw. Theory Techn.*, vol. 69, no. 11, pp. 4961–4976, Nov. 2021.

[51] L. Iotti, G. LaCaille, and A. M. Niknejad, "A dual-injection technique for mm-wave injection-locked frequency multipliers," *IEEE Trans. Microw. Theory Techn.*, vol. 69, no. 12, pp. 5417–5428, Dec. 2021.

[52] M. Richards, *Fundamentals of Radar Signal Processing*, 2nd ed. New York, NY, USA: McGraw-Hill, 2014.

[53] W. J. Rugh, *Nonlinear System Theory: The Volterra/Wiener Approach*. Baltimore, MD, USA: Johns Hopkins Univ. Press, 1981.

[54] J. J. Bussgang, L. Ehrman, and J. W. Graham, "Analysis of nonlinear systems with multiple inputs," *Proc. IEEE*, vol. 62, no. 8, pp. 1088–1119, Aug. 1974.